The significant impact of aerosol vertical structure on lower-atmosphere stability and its critical role in aerosol-PBL interactions

Tianning Su[1], Zhanqing Li[1]*, Chengcai Li[2], Jing Li[2], Wenchao Han[1,3], Chuanyang Shen[2,4], Wangshu Tan[2], Jing Wei[1,3], Jianping Guo[5]

[1]Department of Atmospheric and Oceanic Sciences & ESSIC, University of Maryland , College Park, Maryland 20740, USA

[2]Department of Atmospheric and Oceanic Sciences, Peking University, Beijing 100871, China

[3]State Key Laboratory of Remote Sensing Science and College of Global Change and Earth System Science, Beijing Normal University, 100875, Beijing, China

[4]Department of Earth, Atmospheric and Planetary Sciences, Massachusetts Institute of Technology, Cambridge, MA, USA

[5]State Key Laboratory of Severe Weather, Chinese Academy of Meteorological Sciences, Beijing 100081, China

∗ Correspondence to: zli@atmos.umd.edu

Abstract. Aerosol-planetary boundary layer (PBL) interaction was proposed as an important mechanism to stabilize the atmosphere and exacerbate surface air pollution. Despite the tremendous progress made in understanding this process, its magnitude and significance still have large uncertainties and vary largely with aerosol distribution and meteorological conditions. In this study, we focus on the role of aerosol vertical distribution on thermodynamic stability and PBL development by jointly using micropulse lidar, sunphotometer, and radiosonde measurements taken in Beijing. Despite the complexity of aerosol vertical distributions, cloud-free aerosol structures can be largely classified into three types: well-mixed, decreasing with height, and inverse structures. The aerosol-PBL relationship and diurnal cycles of the PBL height and $PM_{2.5}$ associated with these different aerosol vertical structures show distinct characteristics. The vertical distribution of aerosol radiative forcing differs drastically among the three types with strong heating in the lower, middle, and upper PBL, respectively. Such a discrepancy in heating rate affects the atmospheric buoyancy and stability differently in the three distinct aerosol structures. Absorbing aerosols have the weak effect of stabilizing the lower atmosphere under the decreasing structure than under the inverse structure. As a result, the aerosol-PBL interaction can be strengthened by the inverse aerosol structure, and can be potentially neutralized by the decreasing structure. Moreover, aerosols can both enhance and suppress the PBL stability, leading to both positive and negative feedback loops. This study attempts to improve our understanding of the aerosol-PBL interaction, showing the importance of the observational constraint of aerosol vertical distribution for simulating this interaction

45   and consequent feedbacks.

1. Introduction

Aerosols have a critical impact on the earth's climate through aerosol-cloud interactions (ACI) and aerosol-radiation interactions (ARI). They also continue to contribute toward the considerable uncertainty in quantifying and interpreting the earth's changing radiation budget and hydrological cycles (Charlson et al., 1992; Ackerman et al., 2004; Boucher et al., 2013; Z. Li et al., 2011, 2017a; J. Guo et al., 2017, 2019a). Despite the great advances made in the past decades in observational and modeling studies of aerosol effects, it is still a challenge to accurately quantify aerosol effects on the climate system due to inadequate understanding of some mechanisms and strong variations in aerosol type, loading, and vertical distribution (Haywood and Boucher, 2000; Jacobson et al., 2001; Carslaw et al., 2013; J. Huang et al., 2015; J. Guo et al., 2016a; Z. Li et al., 2016; Wei et al., 2019a, 2019b). Aerosols can interact with thermodynamic stability through ARI (Atwater, 1971; Bond et al., 2013). Absorbing aerosols can stabilize the atmosphere (Ramanathan et al., 2001; Y. Wang et al., 2013; Ding et al., 2016) and may also enhance convection and precipitation under certain conditions (Menon et al., 2002; Z. Li et al., 2017).

Thermodynamic stability in the planetary boundary layer (PBL) dictates the PBL development (Stull, 1988; W. Zhang et al., 2018), thereby dominating the vertical dissipation of surface pollutants to some degree. Aerosols, in turn, have important feedbacks on the stability in the PBL, depending on aerosol properties, especially those of light-absorbing aerosols (e.g., black, organic, and brown carbon). However, due to large uncertainties in aerosol radiative forcing, it remains a challenge to quantify the

impact of aerosols on thermodynamic stability and PBL development. Conventionally,

increasing the aerosol absorption tends to stabilize the atmosphere, leading to a reduced

PBL height (PBLH). A more stable atmosphere and lower PBLH will, in turn, increase

the surface aerosol loading, which is the well-established positive feedback loop in the

aerosol-PBL interaction (e.g., H. Wang et al., 2015; Ding et al., 2016; Petäjä et al., 2016;

Dong et al., 2017; Zou et al., 2017; Q. Huang et al., 2018; Z. Wang et al., 2018; H. Wang

et al., 2019). However, such a positive feedback loop may not be real for all situations

and is subject to confounding factors such as aerosol type, aerosol vertical distribution,

soil moisture, and PBL regime (J. Guo et al., 2019b; Lou et al., 2019). Geiß et al. (2017)

reported the ambiguous relationship between surface aerosol loading and PBLH, while

our previous study revealed weak correlations between surface pollutants and the PBLH

in mountainous or clean regions (Su et al., 2018). Lou et al. (2019) showed that aerosols

have a positive correlation with the PBLH under stable PBL conditions, indicating the

importance of thermodynamic conditions in the PBL.

Among others, numerical models are one of the viable methods used to determine

aerosol impacts on stability and PBL (e.g., J. Wang et al., 2014; Ding et al., 2016; Y.

Wang et al., 2018; Zhou et al., 2018). The aerosol optical depth (AOD), a measure of

aerosol columnar loading, is usually taken into account in model simulations. However,

the aerosol vertical distribution in models is generally prescribed and may differ greatly

from the real situation. With observational constraints, the role of aerosol vertical

distributions in aerosol-PBL interactions warrants further investigation.

Ample observational datasets for Beijing are available, including aerosol vertical

distributions derived from lidar, optical properties derived from the sunphotometer, profiles of meteorological variables from radiosonde (RS), and surface $PM_{2.5}$ and meteorological parameters. Based on these measurements, a radiative transfer model is used to simulate the vertical profiles of aerosol radiative forcing that are employed to investigate the impact of aerosols on buoyancy in the lower atmosphere.

The paper is structured as follows. Section 2 introduces the datasets and methods used. Section 3 presents analyses of aerosol-PBL interactions under different aerosol vertical structures. Section 4 discusses the results with a brief summary.

2. Data and Method

2.1. Site description

We utilized data from multiple sources in Beijing, a megacity located in the North China Plain. As one of the most densely populated and urbanized regions in the world, Beijing is a polluted region with high concentrations of absorbing aerosols (Y. Zhang et al., 2019). The micropulse lidar (MPL) located in Beijing was operated continuously by Peking University (39.99°N, 116.31°E) from March 2016 to December 2018, with a temporal resolution of 15 s and a vertical resolution of 15 m. Due to incomplete laser pulse corrections, the near-surface lidar blind zone is ~0.15 km. Background subtraction, saturation, after-pulse, overlap, and range corrections are applied to raw MPL data to calculate the normalized signals (Yang et al., 2013; Su et al., 2017a). MPL data on raining days are excluded. Level 1.5 AOD and single-scattering albedos (SSA) are employed at multiple wavelengths (i.e., 0.44, 0.5, 0.67, 0.87, and 1.02 μm) from the

112   Beijing RADI (40°N, 116.38°E) Aerosol Robotic Network (AERONET) site from 2011

113   to 2018 under cloud-free conditions (Holben et al., 1998; Smirnov et al., 2000; Y. Zhang

114   et al., 2017). The RS station (39.80°N, 116.47°E) in Beijing, operated by the China

115   Meteorological Administration, is ∼25 km from the MPL site. The variables observed

116   at the RS station include meteorological data and profiles of water vapor, temperature,

117   pressure, and wind. The vertical resolution of the RS is altitude dependent and generally

118   less than 8 m (J. Guo et al., 2016b; W. Zhang et al., 2018). The RS is routinely launched

119   at 0800 Local Time (LT) and 2000 LT each day and is also launched at 1400 LT in the

120   summer (June-July-August). RS measurements are collected during 2011–2018. To

121   reduce small-scale biases and to obtain a picture of the regional variation in particulate

122   matter with the diameter smaller than 2.5 μm (PM$_{2.5}$), we acquire mean PM$_{2.5}$ data from

123   twenty environmental monitoring stations located within 20 km from the lidar site,

124   including one station at the Beijing Embassy of the United States. Figure 1 shows the

125   topography of Beijing. The green square indicates the MPL site, and the yellow triangle

126   indicates the AERONET station. The brown star represents the RS station, and the red

127   pink dots represent the PM$_{2.5}$ sites.

128   **2.2. Statistical analysis methods**

129   The statistical significance is tested by two independent statistical methods, namely,

130   the least-squares regression and the Kendall' tau (MK) test (Mann, 1945; Kendall, 1975;

131   J. Li et al., 2016). Least-squares regression typically assumes a Gaussian data

132   distribution in the trend analysis, whereas the MK test is a nonparametric test without

133   any assumed functional form. The latter is more suitable for data that do not follow a

134 certain distribution. To improve the robustness of the analysis, a relationship is

135 considered significant when the confidence level is above 99% for both the least-

136 squares regression and the MK test. Hereafter, "significant" indicates that the

137 correlation is statistically significant at the 99% confidence level.

138 We primarily use the linear-fit method to build relationships between different

139 parameters. The Pearson correlation coefficient derived from the linear regression

140 analysis measures the degree to which the data fit a linear relationship. However,

141 following our recent work (Su et al., 2018), inverse fitting $[f(x) = A/x + B]$ is used

142 to establish the relationship between PBLH and PM$_{2.5}$. The magnitude of the correlation

143 coefficient ($R^{\dagger}$) is designed to measure the degree to which the data fit an inverse

144 relationship. Since the relationship between the PBLH and PM$_{2.5}$ is non-linear, the

145 inverse fitting better characterizes this relationship.

146 **2.3. PBLH and buoyancy derived from RS**

147 The RS vertical resolution varies according to the balloon ascending rate. The RS

148 records measurements every 1.2 s, which represents an approximate vertical resolution

149 of 5–8 m. Prior to the retrieval of the PBLH, we further resample RS data to achieve a

150 vertical resolution of 5 hPa with linear interpolation. We follow a well-established

151 method developed by Liu and Liang (2010) to derive the PBLH based on profiles of the

152 potential temperature gradient that takes into account different stability conditions. In

153 this study, we only focus on PBLs driven by buoyancy, so PBLs driven by low-level

154 jets are excluded using RS-derived wind profiles (Liu and Liang, 2010; Miao et al.,

155 2018).

156   The static stability of the atmosphere is determined by the buoyancy force, which

157   is expressed as (Wallace and Hobbs, 2006)

158
$$B = \frac{d^2z}{dt^2} = \frac{T' - T}{T}g = -g\Delta z \frac{1}{\theta}\frac{d\theta}{dz} \quad , \qquad (1)$$

159   where z is the height of the air parcel, and t indicates the time. T' represents the

160   temperature of the parcel, T represents the temperature of the environment, and θ is

161   the virtual potential temperature of the environment. An atmospheric layer is convective

162   if the buoyancy is above zero and stable when the buoyancy is below zero. If the

163   buoyancy is near zero, the atmosphere is neutral. We calculated buoyancy with a

164   vertical resolution of 30m. Based on the identification method for PBL type (Liu and

165   Liang, 2010; W. Zhang et al., 2018), we present profiles of buoyancy forcing for stable,

166   neutral, and convective PBLs (Figure 2a). Results shown are averages from 3069

167   radiosonde measurements, of which 438 cases are convective PBLs, 714 cases are

168   neutral PBLs, and 1916 cases are stable PBLs. The strongest upward or downward

169   forcing occurs near the surface. Figures 2b-c further show the height-dependent

170   correlation coefficients between buoyancy and PBLH/PM$_{2.5}$ with an interpolation

171   window of 0.2 km. Note that the PBLH and surface PM$_{2.5}$ are fixed for the entire column,

172   and the buoyancy is height dependent. Due to the insufficient development of the PBL,

173   we do not use RS data at 0800 LT here. To exclude the impact induced by the dragging

174   effects of rainfall, we only consider cases without precipitation within the past 24 hours.

175   Strong upward buoyancy can uplift the PBLH and mitigate surface pollutants,

176   especially in the lower atmosphere. Thus, we vertically average the buoyancy forcing

177   profiles within the lowest 1 km (red line in Figures 2b-c), defined as the lower-

atmosphere buoyancy (LAB). As shown in Figures 3a-b, LAB and PM$_{2.5}$ are negatively

correlated, and LAB and PBLH are positively correlated. LAB also has a significant

negative correlation with absorbing aerosol optical depth (Figure 3c). This may be due

to the stabilizing effect of absorbing aerosols on the atmosphere, widely reported in

many previous studies (H. Wang et al., 2015; Ding et al., 2016; Petäjä et al., 2016; Dong

et al., 2017; Z. Li et al., 2017b; X. Huang et al., 2018).

2.4. PBLH and aerosol extinction coefficient derived from MPL

MPL data from Beijing were used to retrieve the PBLH during the daytime (0800–

1900 LT). Many methods have been developed for retrieving the PBLH from MPL

measurements, e.g., the signal threshold (Melfi et al., 1985), the maximum of the signal

variance (Hooper and Eloranta, 1986), the minimum of the signal profile derivative

(Flamant et al., 1997), and the wavelet transform (Cohn and Angevine, 2000; Davis et

al., 2000; Su et al., 2017b; Chu et al., 2019). To derive the PBLH from MPL data, we

adopted previous well-established approaches with several refinements, which have

already been validated by long-term data collected at the Southern Great Plains site

(Sawyer and Li, 2013; Su et al., 2020).

We initially identify the local maximum positions (range: 0.25–4 km) in the

covariance transform function collocated with a signal gradient larger than a certain

threshold. We further estimated the shot noise (σ) induced by background light and dark

currents for each profile, and then set the threshold as 3σ. The initial PBLH retrieval

(at 0800 LT) is constrained by the PBLH value derived from the morning RS sounding.

Then, the following PBLHs are retrieved using a stability-dependent model based on

200   continuity. Boundary layer clouds are identified to diagnose the PBLH for cloudy cases.

201   Figure 3d presents the comparison of summertime PBLH results derived from MPL and

202   RS at 1400 LT, showing good agreement (R = 0.79).

203   Multiple studies have provided a well-established algorithm to retrieve the vertical

204   profiles of aerosol extinction coefficient (AEC) from MPL data (e.g., Fernald, 1984;

205   Klett, 1985; Liu et al., 2012). The Klett method is further used to retrieve extinction

206   profiles (Klett, 1985). The column-averaged extinction-to-backscatter ratio (the so-

207   called lidar ratio) is an important parameter in the retrieval process and is constrained

208   using AERONET-derived AOD at 0.5 μm. The AEC is assumed to be equal within the

209   blind zone. The overall uncertainties from the overlap function, the lidar ratio, the

210   effects of multiple scattering, and noise fall within the range of 20–30% in the retrieval

211   process (He et al., 2006).

212   **2.5. Estimation of the impacts of aerosols on buoyancy**

213   To show vertical profiles of aerosol radiative forcing, the Santa Barbara DISORT

214   Atmospheric Radiative Transfer (SBDART) model (Ricchiazzi et al., 1998) was used

215   to simulate the atmospheric heating rate (dT/dt) induced by aerosols (Liu et al., 2012;

216   Dong et al., 2017). Integrated aerosol inputs include AODs, SSAs (i.e., at 0.44, 0.67,

217   0.87, and 1.02 μm) retrieved from AERONET measurements, and AEC profiles at 0.5

218   μm obtained from the MPL. We also use Moderate Resolution Imaging

219   Spectroradiometer surface reflectances as an additional input

220   (https://modis.gsfc.nasa.gov/data/dataprod/mod09.php). We further use heating rates

221   induced by aerosols to estimate the impact of aerosols on buoyancy.

222   Theoretically, the rate of change in buoyancy for a certain layer is expressed as

223
$$\frac{dB}{dt} = \frac{d}{dt}\left(\frac{T_0 - \Gamma_d \Delta z - T}{T} g\right) = \frac{\left(\frac{dT_0}{dt} - \frac{dT}{dt}\right)T + \frac{dT}{dt}(\Gamma_d - \Gamma)\Delta z}{T^2} g \quad , \qquad (2)$$

224   where most parameters are defined in the same way as in Eq. (1), and Γ_d (Γ)

225   represents the dry adiabatic lapse rate (environmental lapse rate). We primarily focus

226   on the rate of change in buoyancy during the noontime period (1100–1500 LT), when

227   the PBL is well developed, and aerosol radiative forcing is strong. The rate of change

228   in buoyancy (dB/dt) induced by aerosols is largely determined by the aerosol heating

229   rate, which can be produced by the radiative transfer model. Additional inputs include

230   the environmental lapse rate and temperature, obtained from noontime RS soundings in

231   the summer. For other times, the environmental lapse rate and temperature are obtained

232   from MERRA-2 reanalysis data, which assimilates coarse-resolution RS observations

233   (Rienecker et al., 2011). In this way, we can estimate dB/dt induced by aerosols with

234   a primary focus on the daytime. Note that the errors in MERRA-2 data lead to

235   uncertainties in the estimated dB/dt. A 1–3 K uncertainty in MERRA-2 temperatures

236   (Gelaro et al., 2017) leads to 1–3% relative biases in the estimated dB/dt. Considering

237   the large variation in dB/dt for different aerosol structures, the biases resulting from

238   MERRA-2 data are not a serious issue.

239

3. Results

3.1. Classification of different aerosol structure scenarios

By altering the adiabatic heating rate of the atmosphere, the aerosol vertical distribution is of great importance to the PBL. Based on cloud-free AEC profiles in the PBL, aerosol vertical structures can be classified into three types: well-mixed, decreasing with height, and its inverse, increasing with height. If AEC varies by less than 20% within the lowest 80% of the PBL, it is considered a well-mixed structure. For the other cases, a decreasing structure indicates a peak in AEC near the surface, and the inverse structure indicates a peak in AEC in the middle or upper PBL.

To investigate the vertical variation in AEC within the PBL, the evolution of the PBLH has to be taken into account. Following previous studies (Ferrero et al., 2014; Kuang et al., 2017), vertical profiles were normalized by introducing a standardized height (H_s), calculated as follows:

$$H_s = \frac{z - PBLH}{PBLH} \ , \qquad (3)$$

where z is the height above the ground, and H_s is 0 at the PBL top and -1 at ground level. Figure 4 shows the normalized vertical profiles of AEC derived from MPL data for different aerosol structures around noontime. The number of samples and percentages of decreasing, well-mixed, and increasing aerosol structures are 998 (51%), 611 (32%), and 330 (17%), respectively. Since a temperature inversion located at the PBL top traps moisture and aerosols, there is a sharp decrease in the AEC profile from the PBL upper boundary to the free atmosphere. Variations in the aerosol vertical distribution largely depend on different conditions, but share similar features among the

262 different aerosol structure patterns. Despite complex aerosol vertical distributions, these

263 three types of profiles can account for most of the cloud-free cases.

264 **3.2. PBLH and PM$_{2.5}$ under different aerosol structure scenarios**

265 Absorbing aerosols tend to have a positive feedback with the PBLH, and the

266 aerosol vertical distribution plays a critical role in this process. We investigate the

267 relationship between MPL-derived PBLH and PM$_{2.5}$ for absorbing (daily average

268 SSA ≤ 0.85) or weakly absorbing (daily average SSA > 0.9) aerosols for

269 increasing/decreasing aerosol structures during 0900–1900 LT (Figure 5). The PBLH-

270 PM$_{2.5}$ relationships can represent the intensity of the aerosol-PBL interaction. In general,

271 there are stronger correlations between PBLH and PM$_{2.5}$ for the inverse aerosol

272 structure. This is likely caused by substantial heating in the upper PBL, facilitating the

273 formation of a temperature inversion and further increasing the stability of the PBL.

274 For the decreasing aerosol structure, aerosols may not significantly redistribute

275 adiabatic energy. Hence, the PBLH-PM$_{2.5}$ correlation is relatively weak. Significant

276 PBLH-PM$_{2.5}$ correlations are found for both absorbing and weakly absorbing cases,

277 indicating that scattering aerosols may also play an important role in the aerosol-PBL

278 interaction, especially for the inverse aerosol structure.

279 Figure 6 presents the averaged diurnal cycles of AEC, PBLH, and PM$_{2.5}$ for

280 different aerosol vertical structures, classified based on the average AEC profiles during

281 noontime. High humidity cases (surface relative humidity > 90%) and strong wind cases

282 (wind speed > 5m s^{-1}) are excluded. Here, both AEC and PBLH are derived from MPL

283 data. Data are collected on 371 available days, of which 191 days have decreasing

284   aerosol structures, 122 days have well-mixed aerosol structures, and 58 days have

285   inverse aerosol structures. Multiple entangled factors can contribute to the formation of

286   different aerosol structures within the PBL, including synoptic patterns, new particle

287   formation, vertical turbulence, horizontal transport, entrainment rates, to name a few.

288   In general, the inverse structure is characterized by higher aerosol loadings and lower

289   PBLHs, whereas the decreasing structure is characterized by light pollution and a well-

290   developed PBL. In theory, $PM_{2.5}$ should generally decrease with increasing PBLH in

291   the morning due to the dilution effect. This situation is demonstrated clearly for

292   decreasing aerosol structures. However, $PM_{2.5}$ continuously grows during the daytime

293   when an inverse aerosol structure is present, regardless of the PBLH diurnal cycle. Even

294   though many factors control the diurnal variations in aerosols and the PBL, the strong

295   aerosol-stability interaction generates an unfavorable condition for the vertical

296   dissipation of aerosols, so the surface aerosol loading can continuously accumulate due

297   to emissions.

298   The correlations and statistical results concerning the PBLH and $PM_{2.5}$ provide

299   hints about the differences in aerosol-PBL interactions for different aerosol structures.

300   However, these results cannot explain the feedback loop and causality. Therefore, we

301   further use the SBDART model with the constraint of ample observations to investigate

302   the vertical profiles of radiative forcing induced by aerosols and its impacts on

303   atmospheric stability.

3.3. Aerosol radiative forcing for different aerosol structures

304

305   Following the description in Section 2.5, we calculate the statistical means of

aerosol radiative forcing in the vertical for decreasing, well-mixed, and inverse aerosol structures, derived from the cases presented in Figure 6. Figure 7 shows that the vertical distributions of the heating rate differ drastically among the different aerosol structures. For the inverse aerosol structure scenario, aerosols cause substantial heating in the upper PBL, facilitating the formation of a temperature inversion and further increasing the stability in the PBL. For the decreasing aerosol structure scenario, the abundance of aerosols at the bottom of PBL heats the lower PBL so can potentially enhance convection in the PBL.

There are considerable differences in heating rate among the three distinct aerosol structures (Figure 8), which affects the atmospheric buoyancy and stability differently. On average, aerosols generally suppress buoyancy in the lower atmosphere. Such an effect is quite notable for the inverse structure and is insignificant for the decreasing structure with large standard deviations. Absorbing aerosols are not very helpful for stabilizing the lower atmosphere when a decreasing aerosol structure is present, but they play an important role when an inverse aerosol structure is present. As such, we expect the strongest aerosol-PBL interaction to occur for absorbing aerosol cases when an inverse aerosol structure is present, consistent with the results shown in Figure 5.

Figure 9 shows schematic diagrams of the interactions between aerosols, stability, and the PBL when decreasing/inverse aerosol structures are present. Overall, both decreasing and inverse aerosol structures can cool the surface and suppress sensible heat, thus stabilizing the PBL. In both cases, aerosols have notable stabilizing effects near the surface.

328  When a decreasing aerosol structure is present, abundant aerosols near the surface

329 generate a stronger aerosol heating rate in the lower PBL than in the upper PBL. Such

330 aerosol radiative forcing lowers the potential temperature gradient ($d\theta/dz$) in the

331 middle and upper PBL and can further strengthen vertical convection in the middle and

332 upper PBL. The opposite aerosol effects on PBL stability lead to a relatively weak

333 aerosol feedback and a relatively weak aerosol-PBL interaction. When an inverse

334 aerosol structure is present, the significant heating effect on the upper PBL facilitates

335 the formation of temperature inversion and further increases the stability and suppresses

336 the PBLH. The notable increase in stability lead to the strong, positive aerosol feedback.

337  Highly variable aerosol vertical distributions cause large variations in the impact

338 of aerosol on stability, and thus, exert important and highly variable influences on the

339 aerosol-PBL interactions. Although aerosol stabilize PBL for majority cases, aerosol

340 also can suppress the stability in low-atmosphere when aerosol heating effect is much

341 stronger on the near surface than upper PBL, and further lead to a potential negative

342 feedback loop. The positive feedback loop leads to strong aerosol-PBL interactions,

343 whereas negative feedback loop leads to weak aerosol-PBL interactions. It explains the

344 paradox of the different correlations between PBLH and surface pollutants since its

345 magnitude, significance, and even sign reportedly varies or even reverses (Quan et al.,

346 2013; Tang et al., 2015; Geiß et al., 2017; Su et al., 2018).

347

348 **4. Summary and Discussion**

349  Based on integrated aerosol and meteorological measurements made in Beijing, the

aerosol-PBL interaction is assessed for different aerosol vertical structures, i.e., decreasing, well mixed, and inversely increasing with height. The aerosol-PBL relationships and the diurnal cycles of PBLH and $PM_{2.5}$ show distinct characteristics among the different aerosol vertical patterns. For the decreasing aerosol structure, $PM_{2.5}$ decreases in the morning with relatively large PBLH growth rates. In this situation, absorbing aerosols are not very helpful in stabilizing the lower atmosphere. For the inverse aerosol structure, $PM_{2.5}$ continuously grows during the daytime with relatively low PBLH growth rates. This phenomenon could be a sign of a strong aerosol-PBL interaction. The aerosol radiative forcing in the vertical for decreasing, well-mixed, and inverse aerosol structures differ drastically with strong heating in the lower, middle, and upper PBL, respectively. Such a difference in heating rate affects the atmospheric buoyancy and stability differently in the three distinct aerosol structures.

Turbulent fluxes and eddies in the PBL would spread out and redistribute the radiative effects induced by aerosols. Needed are numerical models to quantify the aerosol-PBL interaction and consequent feedbacks (e.g., Y. Wang et al., 2013; Ding et al., 2016; Z. Wang et al., 2018; Zhou et al., 2018). Aerosol vertical distributions greatly vary on both temporal and vertical scales and critically affect aerosol radiative effects. However, the aerosol vertical distribution is still poorly represented in numerical models, partly due to a lack of observational constraints. This study reveals the important role of the aerosol vertical distribution in the aerosol-PBL interaction, which should be carefully taken into account in both observational analyses and model simulations.

372   This study used column-averaged aerosol properties from AERONET. However,

373   the vertical variations in SSA and aerosol type remains unknown, inducing uncertainties

374   in the estimation of aerosol effects. In the future, we plan to use aircraft data from field

375   campaigns to better account for the influence of different types of aerosols with

376   different properties.

377

378   *Data availability.* Hourly PM$_{2.5}$ data are released by the Ministry of Environmental

379   Protection of China (http://113.108.142.147:20035/emcpublish). MERRA-2 reanalysis

380   data   are   publicly   available   at

381   https://disc.gsfc.nasa.gov/datasets?keywords=merra%202&page=1. AERONET data

382   are publicly available at https://aeronet.gsfc.nasa.gov. Meteorological data are provided

383   by the data center of the China Meteorological Administration (http://data.cma.cn/en).

384   Other data used in this study are available upon the request from the leading author

385   (tianning@umd.edu).

386

387   *Author contribution.* T. S. and Z. L. conceptualized this study. T. S. carried out the

388   analysis, with comments from other co-authors. C. L., J. L., and W. T. carried out the

389   MPL observations. J. G. provided auxiliary data. W. H., C. S., W. T., J. W., and J. G.

390   provided useful suggestions for the study. T. S. and Z. L. interpreted the data and wrote

391   the manuscript with contributions from all co-authors.

392

Competing interests. The authors declare that they have no conflict of interest.

394

Acknowledgements. This study is supported by the Department of Energy (DOE) Atmospheric System Research program (DE-SC0018996) and the National Science Foundation (AGS1837811 and AGS1534670). The authors would like to acknowledge Prof. Zhengqiang Li for his effort in establishing and maintaining the Beijing RADI AERONET site. We thank the provision of $PM_{2.5}$ data by the Ministry of Environmental Protection of the People's Republic of China and also thank the provision of meteorological and radiosonde data by the China Meteorological Administration. We extend sincerest thanks to the MERRA team for their datasets.

403

References

Ackerman, A. S., Kirkpatrick, M. P., Stevens, D. E., and Toon, O. B.: The impact of humidity above stratiform clouds on indirect aerosol climate forcing. Nature, 432, 1014–1017. https://doi.org/10.1038/nature03174, 2004.

Atwater, M. A.: The radiation budget for polluted layers of the urban environment. Journal of Applied Meteorology, 10(2), 205–214, 1971.

Bond, T. C., Doherty, S. J., Fahey, D. W., Forster, P. M., Berntsen, T., DeAngelo, B. J., Flanner, M. G., Ghan, S., Kärcher, B., Koch, D. and Kinne, S.: Bounding the role of black carbon in the climate system: A scientific assessment. Journal of Geophysical Research: Atmospheres, 118(11), 5380–5552, 2013.

Boucher, O., Randall, D., Artaxo, P., Bretherton, C., Feingold, G., Forster, P., Kerminen, V. M., Kondo, Y., Liao, H., Lohmann, U., and Rasch, P.: Clouds and aerosols, in: Climate Change 2013: The Physical Science Basis. Contribution of Working Group I to the Fifth Assessment Report of the Intergovernmental Panel on Climate Change, 571–657, Cambridge Univ. Press, Cambridge, UK and New York, NY, USA, 2013.

Carslaw, K.S., Lee, L.A., Reddington, C.L., Pringle, K.J., Rap, A., Forster, P.M., Mann, G.W., Spracklen, D.V., Woodhouse, M.T., Regayre, L.A. and Pierce, J.R.: Large contribution of natural aerosols to uncertainty in indirect forcing. Nature, 503(7474), p.67, 2013.

Charlson, R.J., Schwartz, S.E., Hales, J.M., Cess, R.D., Coakley, J.J., Hansen, J.E. and Hofmann, D.J.: Climate forcing by anthropogenic aerosols. Science, 255(5043), pp.423-430, 1992.

Chu, Y., Li, J., Li, C., Tan, W., Su, T. and Li, J.: Seasonal and diurnal variability of planetary boundary layer height in Beijing: Intercomparison between MPL and WRF results. Atmospheric Research, 227, pp.1-13. https://doi.org/10.1175/1520-0450(2000)039<1233:BLHAEZ>2.0.CO;2, 2000, 2019.

Cohn, S. A. and Angevine, W. M.: Boundary layer height and entrainment zone thickness measured by lidars and wind-profiling radars, J. Appl. Meteorol., 39, 1233–1247, 2000.

Davis, K. J., Gamage, N., Hagelberg, C. R., Kiemle, C., Lenschow, D. H., and Sullivan P. P.: An objective method for deriving atmospheric structure from airborne lidar observations. J. Atmos. Ocean. Tech., 17, 1455–1468, https://doi.org/10.1175/1520- 0426(2000)017<1455:AOMFDA>2.0.CO;2, 2000

Deardorff, J. W., G. E. Willis, and B. H. Stockton.: Laboratory studies of the entrainment zone of a convectively mixed layer. J. Fluid. Mech., 100, 41–64, doi: 10.1017/ S0022112080001000, 1980.

Ding, A.J., Huang, X., Nie, W., Sun, J.N., Kerminen, V.M., Petäjä, T., Su, H., Cheng, Y.F., Yang, X.Q., Wang, M.H. and Chi, X.G.: Enhanced haze pollution by black carbon in megacities in China. Geophysical Research Letters, 43(6), pp.2873-2879, 2016.

Dong, Z., Li, Z., Yu, X., Cribb, M., Li, X., and Dai, J.: Opposite long-term trends in aerosols between low and high altitudes: a testimony to the aerosol–PBL feedback, Atmos. Chem. Phys., 17, 7997–8009, https://doi.org/10.5194/acp-17- 7997-2017, 2017.

Fernald, F.G.: Analysis of atmospheric lidar observations: some comments. Applied optics, 23(5), pp.652-653, 1984.

Ferrero, L., Castelli, M., Ferrini, B.S., Moscatelli, M., Perrone, M.G., Sangiorgi, G., D'Angelo, L., Rovelli, G., Moroni, B., Scardazza, F. and Močnik, G.: Impact of black carbon aerosol over Italian basin valleys: high-resolution measurements along vertical profiles, radiative forcing and heating rate. Atmospheric Chemistry and Physics, 14(18), pp.9641-9664, 2014.

Flamant, C., Pelon, J., Flamant, P.H. and Durand, P.: Lidar determination of the entrainment zone thickness at the top of the unstable marine atmospheric boundary layer. Boundary-Layer Meteorology, 83(2), pp.247-284, 1997.

Geiß, A., Wiegner, M., Bonn, B., Schäfer, K., Forkel, R., Schneidemesser, E.V., Münkel, C., Chan, K.L. and Nothard, R.: Mixing layer height as an indicator for urban air quality?. Atmospheric Measurement Techniques, 10(8), pp.2969-2988, 2017.

Gelaro, R., McCarty, W., Suárez, M.J., Todling, R., Molod, A., Takacs, L., Randles, C.A., Darmenov, A., Bosilovich, M.G., Reichle, R. and Wargan, K.: The modern-era retrospective analysis for research and applications, version 2 (MERRA-2). Journal of Climate, 30(14), pp.5419-5454, 2017.

Guo, J., H. Liu, F. Wang, J. Huang, F. Xia, M. Lou, Y. Wu, J. Jiang, T. Xie, Y. Zhaxi, and Y. Yung.: Three-dimensional structure of aerosol in China: A perspective from

multi-satellite observations, Atmospheric Research, 178–179: pp.580–589, 2016a.

Guo, J., Miao, Y., Zhang, Y., Liu, H., Li, Z., Zhang, W., He, J., Lou, M., Yan, Y., Bian, L., and Zhai, P.: The climatology of planetary boundary layer height in China derived from radiosonde and reanalysis data. Atmospheric Chemistry and Physics, 16, pp.13309–13319, 2016b.

Guo, J., Su, T., Li, Z., Miao, Y., Li, J., Liu, H., Xu, H., Cribb, M. and Zhai, P.: Declining frequency of summertime local-scale precipitation over eastern China from 1970 to 2010 and its potential link to aerosols. Geophysical Research Letters, 44(11), pp.5700-5708, 2017.

Guo, J., Su, T., Chen, D., Wang, J., Li, Z., Lv, Y., Guo, X., Liu, H., Cribb, M. and Zhai, P.: Declining summertime local-scale precipitation frequency over China and the United States, 1981–2012: The disparate roles of aerosols. Geophysical Research Letters, 2019a.

Guo, J., Y. Li, J. Cohen, J. Li, D. Chen, H. Xu, L. Liu, J. Yin, K. Hu, P. Zhai.: Shift in the temporal trend of boundary layer height trend in China using long-term (1979–2016) radiosonde data. Geophysical Research Letters, 46 (11), pp.6080-6089, 2019b.

Haywood, J. and Boucher, O.: Estimates of the direct and indirect radiative forcing due to tropospheric aerosols: A review. Reviews of geophysics, 38(4), pp.513-543, 2000.

He, Q.S., Li, C.C., Mao, J.T., Lau, A.K.H. and Li, P.R.: A study on the aerosol extinction-to-backscatter ratio with combination of micro-pulse LIDAR and MODIS over Hong Kong. Atmospheric Chemistry and Physics, 6(11), pp.3243-3256, 2006.

Holben, B.N., Eck, T.F., Slutsker, I., Tanre, D., Buis, J.P., Setzer, A., Vermote, E., Reagan, J.A., Kaufman, Y.J., Nakajima, T. and Lavenu, F.: AERONET—A federated instrument network and data archive for aerosol characterization. Remote sensing of environment, 66(1), pp.1-16, 1998.

Hooper, W. P. and Eloranta, E. W.: Lidar measurements of wind in the planetary boundary layer – the method, accuracy and results from joint measurements with radiosonde and kytoon, Bound.- Lay. Meteorol., 25, 990–1001, 1986.

Huang, J., J. Guo, F. Wang, Z. Liu, M. -J. Jeong, H. Yu and Z. Zhang.: CALIPSO inferred most probable heights of global dust and smoke layers, Journal of Geophysical Research-Atmospheres, 120(10), pp5085–5100, 2015.

Huang, Q., Cai, X., Wang, J., Song, Y. and Zhu, T.: Climatological study of the Boundary-layer air Stagnation Index for China and its relationship with air pollution. Atmospheric Chemistry and Physics, 18(10), p.7573, 2018.

Huang, X., Wang, Z. and Ding, A.: Impact of Aerosol-PBL Interaction on Haze Pollution: Multiyear Observational Evidences in North China. Geophysical Research Letters, 45(16), pp.8596-8603, 2018.

Jacobson, M.Z.: Strong radiative heating due to the mixing state of black carbon in atmospheric aerosols. Nature, 409(6821), p.695, 2001.

Kendall, M. G.: Rank Correlation Methods, 1–202, Griffin, London, 1975.

Klett, J.D.: Lidar inversion with variable backscatter/extinction ratios. Applied optics, 24(11), pp.1638-1643, 1985.

Kuang, Y., Zhao, C.S., Tao, J.C., Bian, Y.X. and Ma, N.: Impact of aerosol hygroscopic growth on the direct aerosol radiative effect in summer on North China Plain. Atmospheric Environment, 147, pp.224-233, 2016.

Li, J., Li, C., Zhao, C. and Su, T.: Changes in surface aerosol extinction trends over China during 1980－2013 inferred from quality－controlled visibility data. Geophysical Research Letters, 43(16), pp.8713-8719, 2016.

Li, Z., Niu, F., Fan, J., Liu, Y., Rosenfeld, D. and Ding, Y.: Long-term impacts of aerosols on the vertical development of clouds and precipitation. Nature Geoscience, 4(12), p.888, 2011.

Li, Z., W.K.-M. Lau, V. Ramanathan, et al.: Aerosol and monsoon climate interactions over Asia. Rev. of Geophys., 54, 866–929. https://doi.org/10.1002/2015RG000500, 2016.

Li, Z., Rosenfeld, D., and Fan, J.: Aerosols and their Impact on Radiation, Clouds, Precipitation and Severe Weather Events, Oxford Encyclopedia in Environmental Sciences, 10.1093/acrefore/9780199389414.013.126, 2017a.

Li, Z., J. Guo, A. Ding, H. Liao, J. Liu, Y. Sun, T. Wang, H. Xue, H. Zhang, B. Zhu.: Aerosol and boundary-layer interactions and impact on air quality. National Science Review, nwx117. https://doi.org/10.1093/nsr/nwx117, 2017b.

Liu, S. and Liang, X.-Z.: Observed diurnal cycle climatology of planetary boundary layer height, J. Climate, 22, 5790–5809, https://doi.org/10.1175/2010JCLI3552.1, 2010.

Liu, J., Zheng, Y., Li, Z., Flynn, C. and Cribb, M.: Seasonal variations of aerosol optical properties, vertical distribution and associated radiative effects in the Yangtze Delta region of China. Journal of Geophysical Research: Atmospheres, 117(D16), 2012.

Lou, M., J. Guo, L. Wang, H. Xu, D. Chen, Y. Miao, Y. Lv, Y. Li, X. Guo, S. Ma, and J. Li.: On the relationship between aerosol and boundary layer height in summer in China under different thermodynamic conditions. Earth and Space Science, 6(5), pp.887-901, 2019.

Mann, H. B.: Nonparametric tests against trend, Econometrica, 13, 245–259, 1945.

Melfi, S.H., Spinhirne, J.D., Chou, S.H. and Palm, S.P.: Lidar observations of vertically organized convection in the planetary boundary layer over the ocean. Journal of climate and applied meteorology, 24(8), pp.806-821, 1985.

Menon, S., Hansen, J., Nazarenko, L. and Luo, Y.: Climate effects of black carbon aerosols in China and India. Science, 297(5590), pp.2250-2253, 2002.

Miao, Y., Guo, J., Liu, S., Wei, W., Zhang, G., Lin, Y. and Zhai, P.: The climatology of low－level jet in Beijing and Guangzhou, China. Journal of Geophysical Research: Atmospheres, 123(5), pp.2816-2830, 2018.

Petäjä, T., Järvi, L., Kerminen, V.M., Ding, A.J., Sun, J.N., Nie, W., Kujansuu, J., Virkkula, A., Yang, X., Fu, C.B., Zilitinkevich, S., and M. Kulmala.: Enhanced air pollution via aerosol-boundary layer feedback in China. Scientific Reports, 6. https://doi.org/10.1038/srep18998, 2016.

Quan, J., Gao, Y., Zhang, Q., Tie, X., Cao, J., Han, S., Meng, J., Chen, P. and Zhao, D.: Evolution of planetary boundary layer under different weather conditions, and its

555   impact on aerosol concentrations. Particuology, 11(1), pp.34-40, 2013.

556 Ramanathan, V.C.P.J., Crutzen, P.J., Kiehl, J.T. and Rosenfeld, D.: Aerosols, climate,
557   and the hydrological cycle. Science, 294(5549), pp.2119-2124, 2001.

558 Ricchiazzi, P., Yang, S., Gautier, C., and Sowle, D.: SBDART: A research and teaching
559   software tool for planeparallel radiative transfer in the Earth's atmosphere, B. Am.
560   Meteorol.   Soc.,   79,   2101–2114,   https://doi.org/10.1175/1520-
561   0477(1998)079<2101:SARATS>2.0.CO;2, 1998.

562 Rienecker, M.M., Suarez, M.J., Gelaro, R., Todling, R., Bacmeister, J., Liu, E.,
563   Bosilovich, M.G., Schubert, S.D., Takacs, L., Kim, G.K. and Bloom, S.: MERRA:
564   NASA's modern-era retrospective analysis for research and applications. Journal
565   of climate, 24(14), pp.3624-3648, 2011.

566 Sawyer, V., and Li, Z.: Detection, variations and intercomparison of the planetary
567   boundary layer depth from radiosonde, lidar, and infrared spectrometer, Atmos.
568   Environ., 79, 518-528, 2013.

569 Smirnov, A., Holben, B.N., Eck, T.F., Dubovik, O. and Slutsker, I.: Cloud-screening
570   and quality control algorithms for the AERONET database. Remote sensing of
571   environment, 73(3), pp.337-349, 2000.

572 Stull, R. B.: The energetics of entrainment across a density interface. J. Atmos. Sci., 33,
573   1260–1267, doi: 10.1175/1520-0469(1976)033<1260:TEOEAD>2.0.CO;2, 1976.

574 Su, T., Li, J., Li, C., Xiang, P., Lau, A.K.H., Guo, J., Yang, D. and Miao, Y.: An
575   intercomparison of long-term planetary boundary layer heights retrieved from
576   CALIPSO, ground-based lidar, and radiosonde measurements over Hong Kong. J.
577   Geophys. Res. Atmos., 122(7), 3929- 3943, 2017a.

578 Su, T., Li, J., Li, C., Lau, A.K.H., Yang, D. and Shen, C.: An intercomparison of AOD-
579   converted PM2. 5 concentrations using different approaches for estimating aerosol
580   vertical distribution. Atmospheric environment, 166, pp.531-542, 2017b.

581 Su, T., Li, Z. and Kahn, R.: Relationships between the planetary boundary layer height
582   and surface pollutants derived from lidar observations over China: regional pattern
583   and influencing factors. Atmospheric Chemistry and Physics, 18(21), pp.15921-
584   15935, 2018.

585 Stull, R. B.: An Introduction to Boundary Layer Meteorology. Kluwer, 670-680 pp,
586   1988.

587 Su, T., Li, Z. and Kahn, R.: A new method to retrieve the diurnal variability of planetary
588   boundary layer height from lidar under different thermodynamic stability conditions.
589   Remote Sensing of Environment, 237, p.111519, 2020.

590 Tang, G., Zhang, J., Zhu, X., Song, T., Münkel, C., Hu, B., Schäfer, K., Liu, Z., Zhang,
591   J., Wang, L. and Xin, J.: Mixing layer height and its implications for air pollution
592   over Beijing, China. Atmospheric Chemistry and Physics, 16(4), pp.2459-2475,
593   2016.

594 Wallace, J.M. and Hobbs, P.V.: Atmospheric science: an introductory survey (Vol. 92).
595   Elsevier, 2006.

596 Wang, H., Shi, G.Y., Zhang, X.Y., Gong, S.L., Tan, S.C., Chen, B., Che, H.Z. and Li,
597   T.: Mesoscale modelling study of the interactions between aerosols and PBL
598   meteorology during a haze episode in China Jing–Jin–Ji and its near surrounding

region–Part 2: Aerosols' radiative feedback effects. Atmospheric Chemistry and Physics, 15(6), pp.3277-3287, 2015.

Wang, H., Li, Z., Lv, Y., Xu, H., Li, K., Li, D., Hou, W., Zheng, F., Wei, Y. and Ge, B.: Observational study of aerosol-induced impact on planetary boundary layer based on lidar and sunphotometer in Beijing. Environmental Pollution, 252, pp.897-906, 2019.

Wang, J., Wang, S., Jiang, J., Ding, A., Zheng, M., Zhao, B., Wong, D.C., Zhou, W., Zheng, G., Wang, L. and Pleim, J.E.: Impact of aerosol–meteorology interactions on fine particle pollution during China's severe haze episode in January 2013. Environmental Research Letters, 9(9), p.094002, 2014.

Wang, Y., A. Khalizov, M. Levy, R. Zhang.: New directions: Light absorbing aerosols and their atmospheric impacts, Atmos. Environ., 81, pp.713-715, 2013.

Wang, Y., Li, Z., Zhang, Y., Du, W., Zhang, F., Tan, H., Xu, H., Fan, T., Jin, X., Fan, X. and Dong, Z.: Characterization of aerosol hygroscopicity, mixing state, and CCN activity at a suburban site in the central North China Plain. Atmospheric Chemistry and Physics, 18(16), pp.11739-11752, 2018.

Wang, Z., Huang, X. and Ding, A.: Dome effect of black carbon and its key influencing factors: a one-dimensional modelling study. Atmospheric Chemistry and Physics, 18(4), pp.2821-2834, 2018.

Wei, J., Huang, W., Li, Z., Xue, W., Peng, Y., Sun, L., and Cribb.: M. Estimating 1-km-resolution $PM_{2.5}$ concentrations across China using the space-time random forest approach, Remote Sensing of Environment, 231, 111221. https://doi.org/10.1016/j.rse.2019.111221, 2019a.

Wei, J., Li, Z., Sun, L., Peng, Y., Zhang, Z., Li, Z., Su, T., Feng, L., Cai, Z. and Wu, H.: Evaluation and uncertainty estimate of next-generation geostationary meteorological Himawari-8/AHI aerosol products. Science of The Total Environment, 692, pp.879-891, 2019b.

Yang, D., Li, C., Lau, A.K.H. and Li, Y.: Long-term measurement of daytime atmospheric mixing layer height over Hong Kong. Journal of Geophysical Research: Atmospheres, 118(5), pp.2422-2433, 2013.

Zhang, W., J. Guo, Y. Miao, H. Liu, Y. Song, Z. Fang, J. He, M. Lou, Y. Yan, Y. Li, and P. Zhai.: On the summertime planetary boundary layer with different thermodynamic stability in China: A radiosonde perspective. Journal of Climate, 31(4), pp. 1451–1465, 2018.

Zhang, Y., Li, Z., Zhang, Y., Li, D., Qie, L., Che, H. and Xu, H.: Estimation of aerosol complex refractive indices for both fine and coarse modes simultaneously based on AERONET remote sensing products. Atmospheric Measurement Techniques, 10(9), pp.3203-3213, 2017.

Zhang, Y., Y. Li, J. Guo, Y. Wang, D. Chen, and H. Chen.: The climatology and trend of black carbon in China from 12-year ground observations. Climate Dynamics, doi:10.1007/s00382-019-04903-0, 2019.

Zhou, M., Zhang, L., Chen, D., Gu, Y., Fu, T.M., Gao, M., Zhao, Y., Lu, X. and Zhao, B.: The impact of aerosol-radiation interactions on the effectiveness of emission control measures. Environmental Research Letters, 2018.

643 Zou, J., Sun, J., Ding, A., Wang, M., Guo, W. and Fu, C.: Observation-based estimation
644   of aerosol-induced reduction of planetary boundary layer height. Advances in
645   Atmospheric Sciences, 34(9), pp.1057-1068, 2017.

646 **Figures**
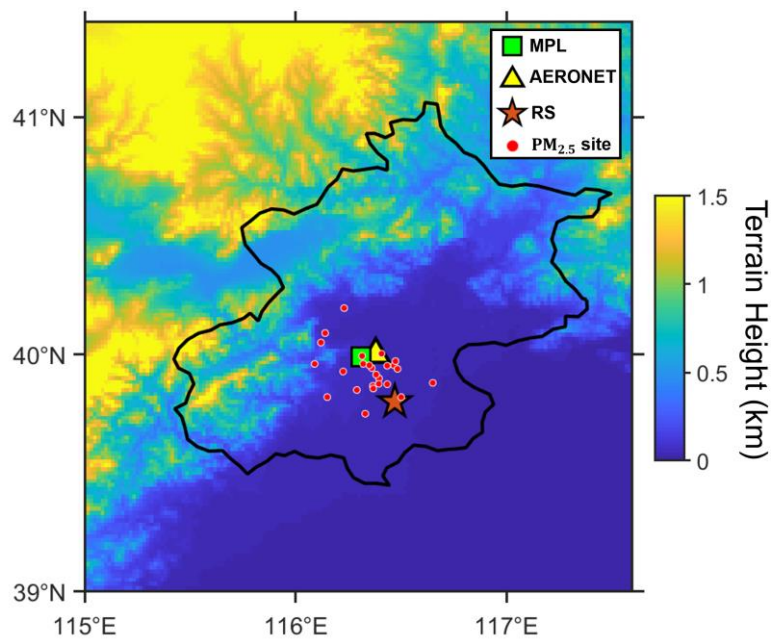
647

648 **Figure 1.** Topography of Beijing. The green square indicates the MPL site, and the

649 yellow triangle indicates the AERONET station. The brown star shows the radiosonde

650 (RS) station, and the red pink dots show the PM$_{2.5}$ sites.

651

652

653

654

655

656

657
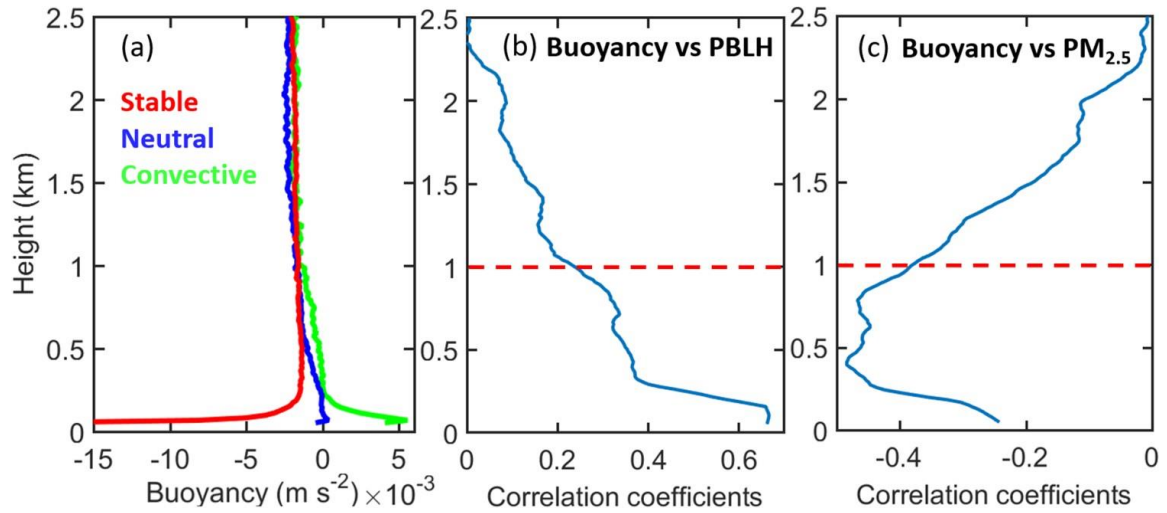
Figure 2. (a) Averaged vertical profiles of buoyancy forcing in stable, neutral, and

convective PBLs. (b) Height-dependent correlation coefficients between buoyancy and

PBLH. (c) Height-dependent correlation coefficients between buoyancy and surface

$PM_{2.5}$. Note that the PBLH and surface $PM_{2.5}$ are fixed for the entire column, and the

buoyancy is height dependent. The buoyancy in the lower atmosphere (< 1 km) has the

most important impact on the PBLH and surface $PM_{2.5}$. The buoyancy and PBLH are

calculated from RS measurements made at 1400 LT and 2000 LT from 2011 to 2018.
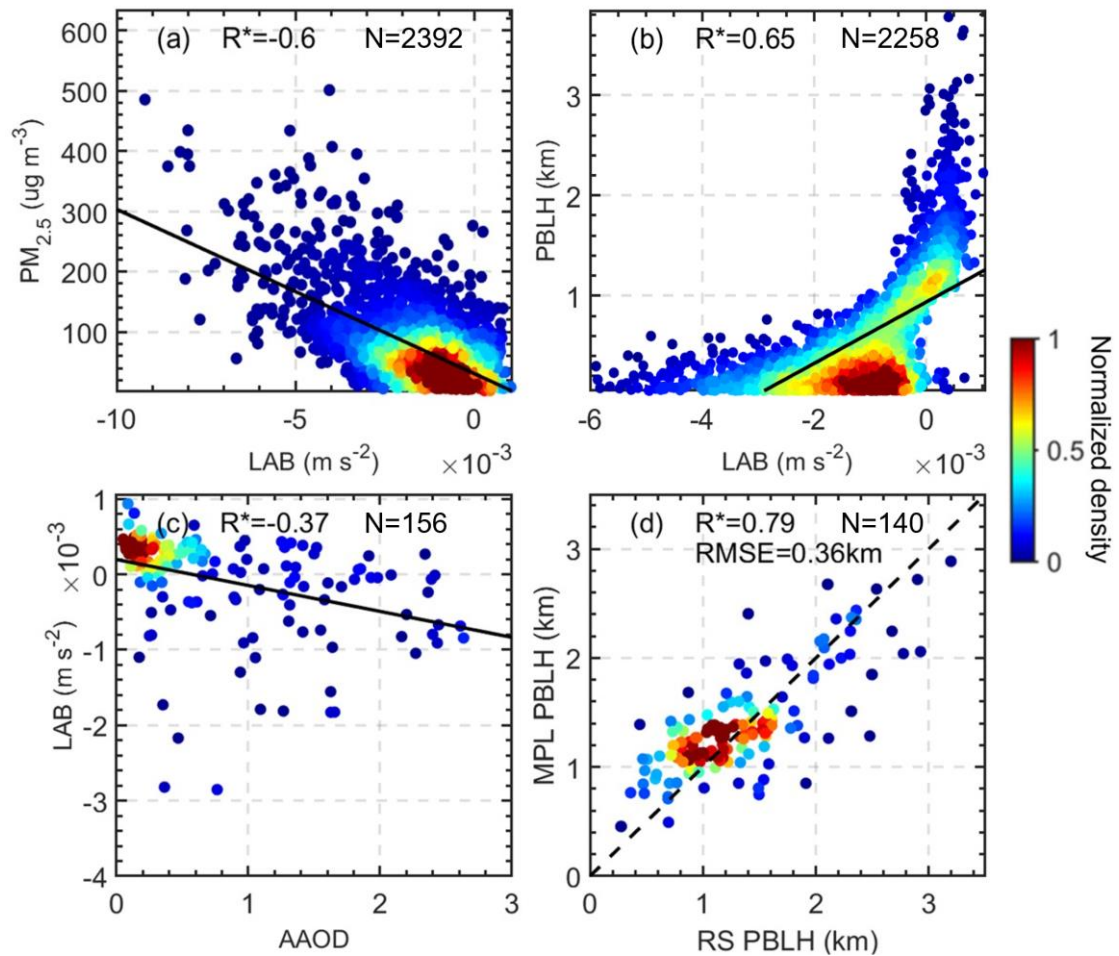
Figure 3. (a) The relationship between lower-atmosphere buoyancy (LAB) and $PM_{2.5}$.

(b) The relationship between LAB and PBLH. (c) The relationship between absorbing

aerosol optical depth (AAOD) and LAB. In (a, b, c), the LAB and PBLH are derived

from RS measurements made at 1400 LT and 2000 LT, and AAOD is derived from

AERONET measurements. The black solid lines indicate the best-fit lines from linear

regression. (d) Comparison of PBLHs derived from the MPL and RS at 1400 LT. Each

panel gives the correlation coefficients (R), sample number (N), and root-mean-square

error (RMSE). R with an asterisk indicates that the correlation is statistically significant

at the 99% confidence level. The color-shaded dots indicate the normalized sample

density.
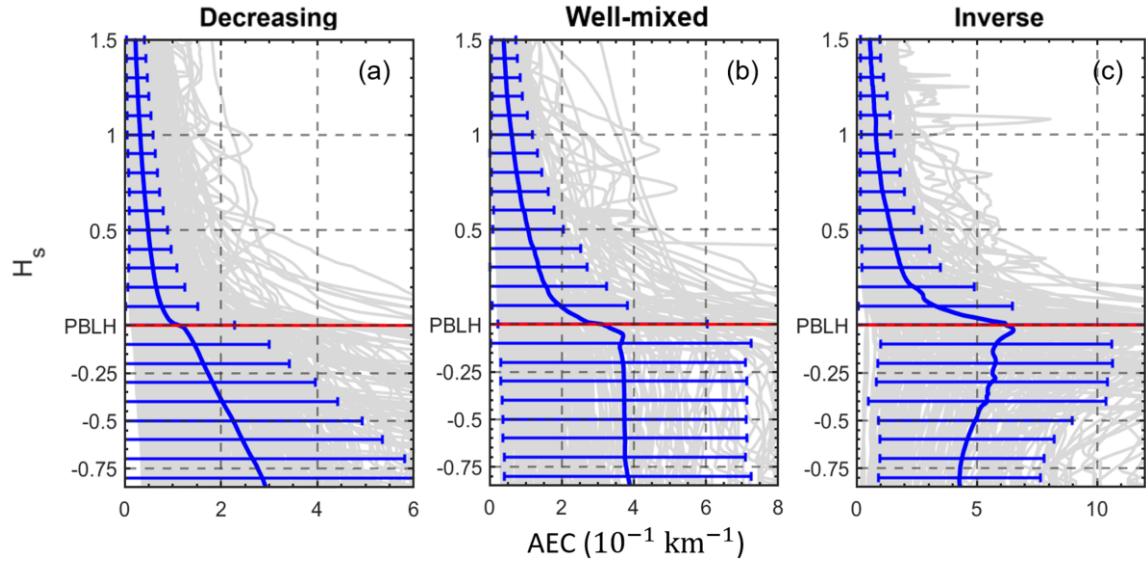
Figure 4. Normalized vertical profiles of aerosol extinction coefficient (AEC) for (a) decreasing, (b) well-mixed, and (c) increasing (i.e., inverse) aerosol structures. Red line mark the position of the PBLH, solid blue lines represent the average profiles of corresponding profiles, and error bars represent the standard deviations.

698
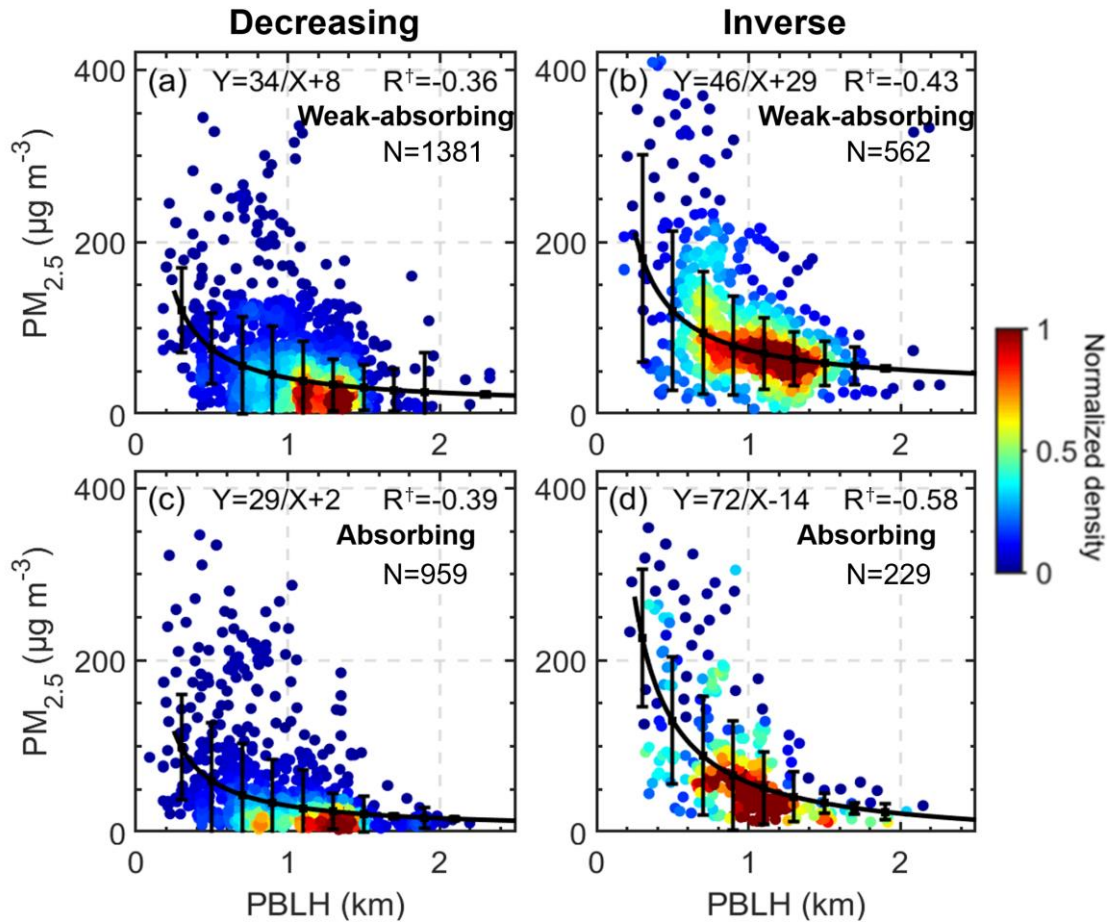
Figure 5. The relationship between MPL-derived PBLH and PM$_{2.5}$ for (a) weakly

absorbing and (c) absorbing aerosols for the decreasing aerosol structure. The

relationship between MPL-derived PBLH and PM$_{2.5}$ for (b) weakly absorbing and (d)

absorbing aerosols for the increasing (i.e., inverse) aerosol structure. Black lines

represent the inverse fits, and the whiskers indicate the standard deviations. The fitting

functions and number of samples are given in each panel, along with the correlation

coefficient ($R^{\dagger}$) for the inverse fit.

706

707
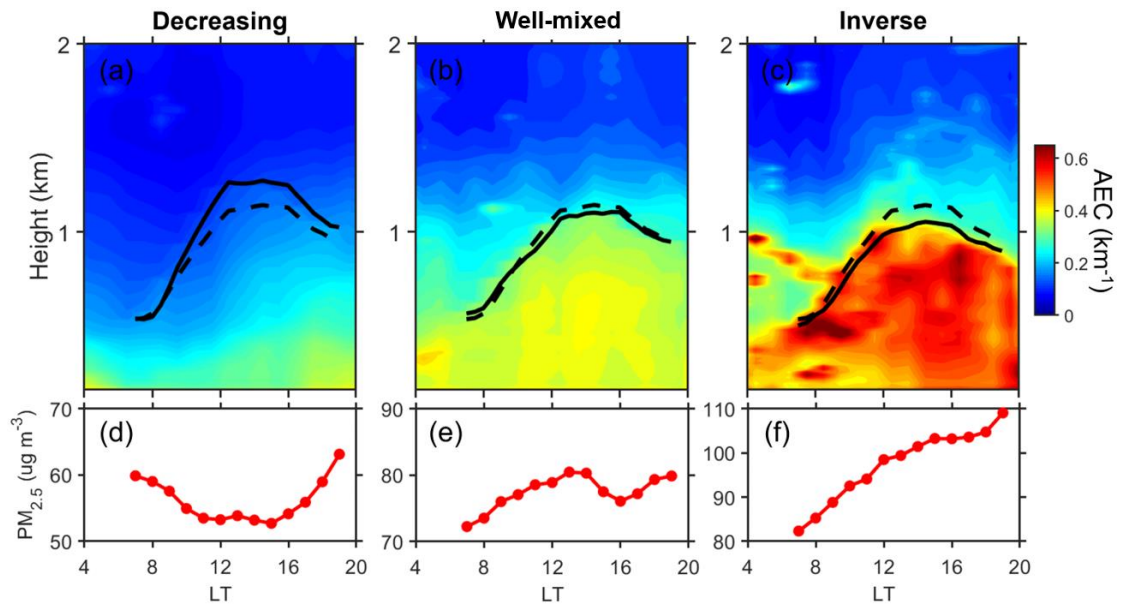
708

709 **Figure 6.** The averaged diurnal variations in AEC for (a) decreasing, (b) well-mixed,

710 and (c) increasing (i.e., inverse) aerosol structures. Solid black lines indicate the

711 averaged diurnal cycles of MPL-derived PBLH under the different aerosol structures.

712 Dashed black lines represent the mean MPL-derived PBLH diurnal cycles. (d, e, f) The

713 averaged diurnal variations in surface $PM_{2.5}$ under the different aerosol structures.

714

715

716

717

718

719

720

721

722
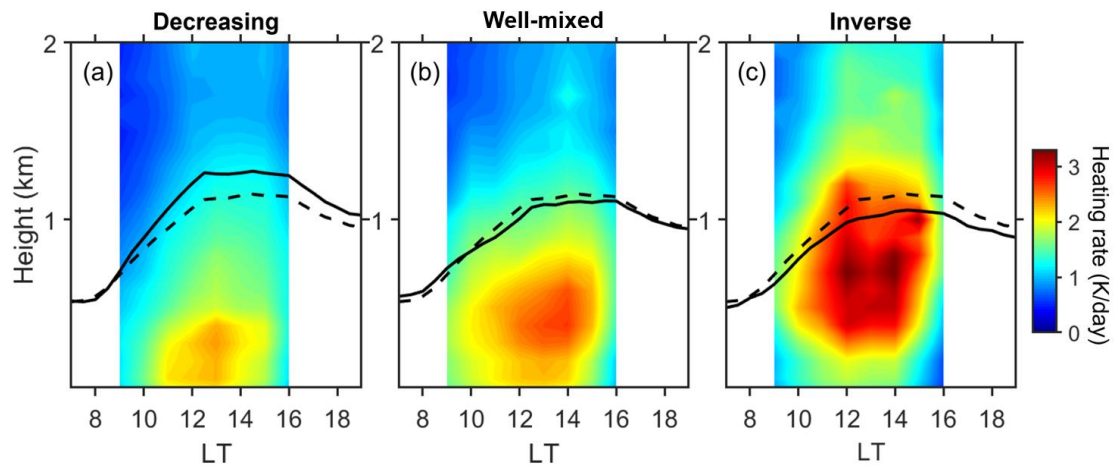
Figure 7. The averaged diurnal variations in aerosol radiative forcing in the vertical for (a) decreasing, (b) well-mixed, and (c) increasing (i.e., inverse) structures of aerosol loading. Solid black lines indicate the mean diurnal cycles of MPL-derived PBLH under different aerosol structures. Dashed black lines represent the mean MPL-derived PBLH diurnal cycles.
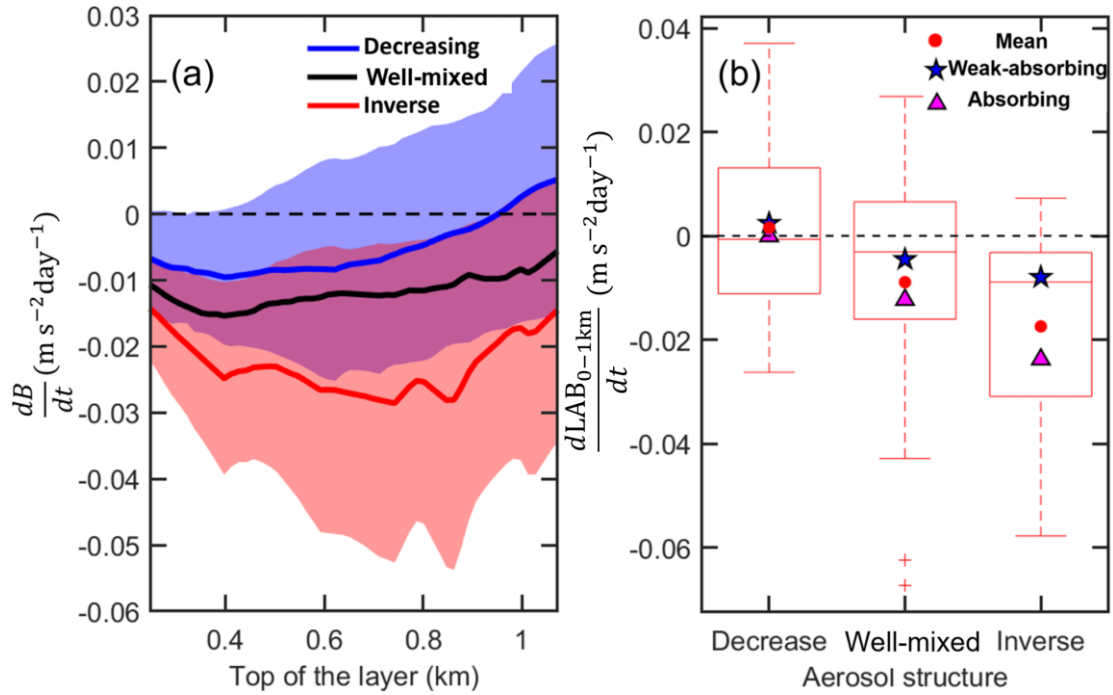
Figure 8. (a) The rate of change in buoyancy (dB/dt) in a layer of the lowest atmosphere for decreasing (blue), well-mixed (black), and inverse (red) aerosol structures during noontime. The bottom of the layer is the surface, and the rate of change in buoyancy is subjected to the top of the layer. The shaded areas show the standard deviations of the rate of change in buoyancy. (b) Box-and-whisker plots showing 10th, 25th, 50th, 75th, and 90th percentile values of the rate of change in LAB_{0-1km} (integrated buoyancy within lowest 1 km) during noontime. Red dots indicate the mean values, and blue stars and pink triangles show the means for weakly absorbing (SSA > 0.9) and absorbing (SSA < 0.85) cases.

751
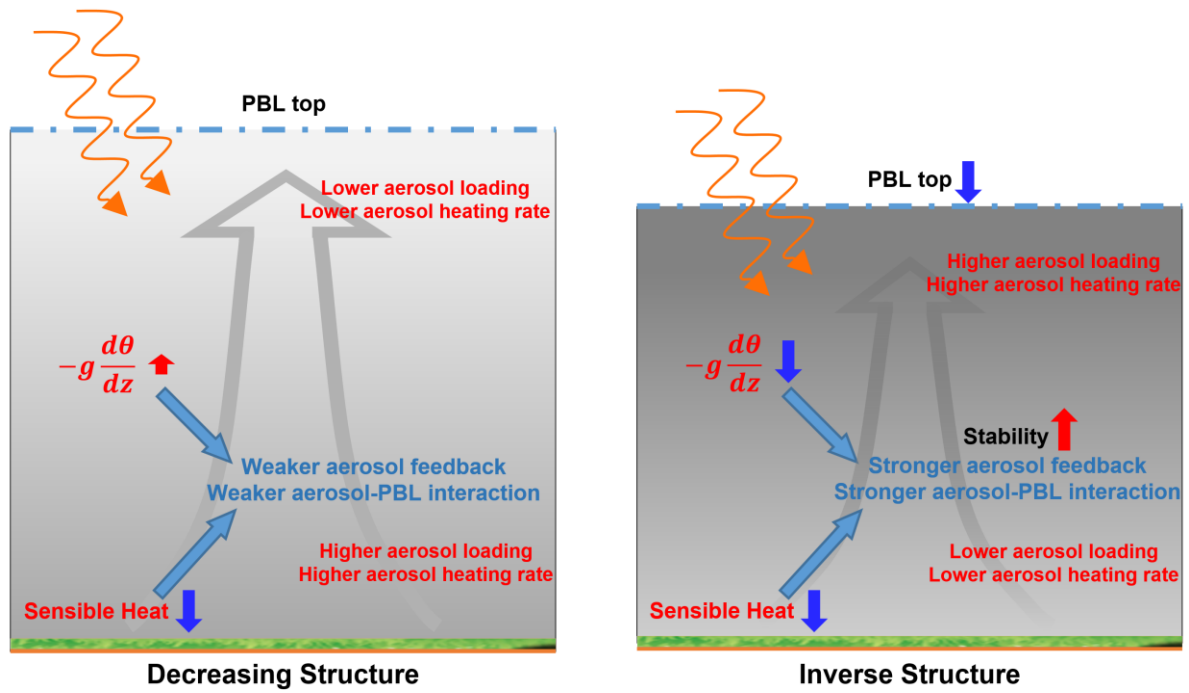
752

753 **Figure 9.** Schematic diagrams describing aerosol-PBL interactions when decreasing

754 and inverse aerosol structures are present. The blue dash-dotted line indicates the top

755 of the PBL. Orange curved arrows indicate solar radiation. The background grey arrow

756 sketches the vertical transport of humidity, aerosols, and heat. The background

757 greyscale indicates the pollution level.

758

759

760

761

762

763

764